

Electrocatalytic Upcycling of Nitrate Wastewater into an Ammonia Fertilizer via an Electrified Membrane

Jianan Gao, Ning Shi, Yifan Li, Bo Jiang,* Taha Marhaba, and Wen Zhang*



Cite This: *Environ. Sci. Technol.* 2022, 56, 11602–11613



Read Online

ACCESS |



Metrics & More



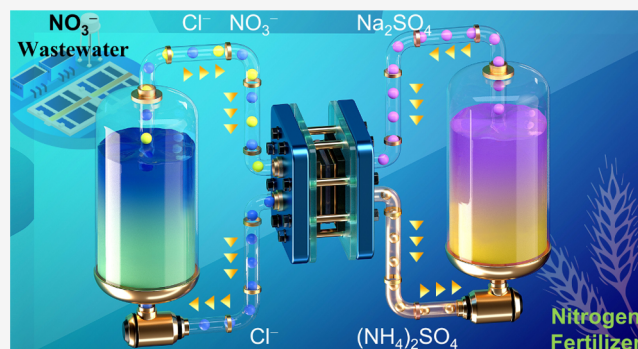
Article Recommendations



Supporting Information

ABSTRACT: Electrochemically upcycling wastewater nitrogen such as nitrate (NO_3^-) and nitrite (NO_2^-) into an ammonia fertilizer is a promising yet challenging research topic in resource recovery and wastewater treatment. This study presents an electrified membrane made of a CuO@Cu foam and a polytetrafluoroethylene (PTFE) membrane for reducing NO_3^- to ammonia (NH_3) and upcycling NH_3 into $(\text{NH}_4)_2\text{SO}_4$, a liquid fertilizer for ready-use. A paired electrolysis process without external acid/base consumption was achieved under a partial current density of $63.8 \pm 4.4 \text{ mA}\cdot\text{cm}^{-2}$ on the cathodic membrane, which removed 99.9% NO_3^- in the feed (150 mM NO_3^-) after a 5 h operation with an NH_3 recovery rate of 99.5%. A recovery rate and energy consumption of $3100 \pm 91 \text{ g}\cdot(\text{NH}_4)_2\text{SO}_4\cdot\text{m}^{-2}\cdot\text{d}^{-1}$ and $21.8 \pm 3.8 \text{ kWh}\cdot\text{kg}^{-1}\cdot(\text{NH}_4)_2\text{SO}_4$, respectively, almost outcompete the industrial ammonia production cost in the Haber–Bosch process. Density functional theory (DFT) calculations unraveled that the *in situ* electrochemical conversion of Cu^{2+} into Cu^{+} provides highly dynamic active species for NO_3^- reduction to NH_3 . This electrified membrane process was demonstrated to achieve synergistic nitrate decontamination and nutrient recovery with durable catalytic activity and stability.

KEYWORDS: electrified membrane flow-cell, paired electrolysis method, nitrate reduction, ammonia recovery, separation science



1. INTRODUCTION

The Haber–Bosch process has long been employed to produce industrial ammonium for fertilization, which consumes fossil fuels to drive the thermodynamically unfavorable reaction between nitrogen (N_2) and hydrogen (H_2) at high pressures and temperatures.^{1,2} Meanwhile, the extensive use of fertilizers and industrial waste streams causes eutrophic water pollution (e.g., with a high nitrate/nitrite content).^{3–5} Conventional biological nitrogen removal involves energy intensive nitrification and denitrification processes (~ 11.7 to $12.5 \text{ kWh}\cdot\text{kg}\cdot\text{N}^{-1}$) that eventually convert all nitrogen species into nitrogen gas.^{6–8} Clearly, shortening the nitrogen removal processes by converting wastewater nitrate into NH_3 can potentially reduce the energy and carbon footprints and enable nutrient recovery and reuse/recycle.^{9–11}

Most previous studies involving nitrogen recovery employed ammonium (NH_4^+)-containing wastewater.^{12–14} The $\text{NO}_3^-/\text{NO}_2^-$ recovery is largely ignored and unexplored probably because they are regarded as pollutants rather than resources. For instance, biological nitrogen removal utilizes denitrification that produces N_2 in wastewater treatment plants. However, NO_3^- could be an ideal nitrogen-containing alternative to replace the most commonly used nitrogen (N_2) as the nitrogen source for NH_3 production due to the relatively low dissociation energy of the $\text{N}=\text{O}$ bond (204 kJ mol^{-1})

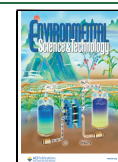
compared with that of the $\text{N}\equiv\text{N}$ bond (941 kJ mol^{-1}). Abundant NO_3^- -laden wastewater are discharged from agricultural and industrial sources, which could release up to 0.9 – 41.6 mM nitrate from polluted groundwater and textile wastewater^{15,16} and 71 – 550 mM from metal finishing, ion exchange brine, and uranium purification wastewater.^{17–19} The annual discharge of nitrate nitrogen in all of the US industrial wastewater is estimated to be 2.4 billion kg.¹¹ Thus, upcycling of this nitrogen resource via electrocatalytic reduction is pivotal for both wastewater treatment and valorization.^{20–22} Therefore, many efforts are recently focused on developing catalytic materials such as strained Ru nanoclusters,²³ CuNi alloy,²⁴ organic molecular solid 3,4,9,10-perylenetetracarboxylic dihydride (PTCDA)-modified Cu,²⁰ and TiO_{2-x} nanotubes²⁵ to selectively boost the electrochemical reduction of NO_3^- to NH_4^+ . For the practical applications of this process, it is essential to separate NH_4^+ to promote electrode surface reactions and avoid product inhibition on electrochemical

Received: December 9, 2021

Revised: July 1, 2022

Accepted: July 8, 2022

Published: July 21, 2022



reactions. Fortunately, NO_3^- reduction generates 1.125 OH^- per mole- e^- alkalinity and results in a localized alkaline microenvironment near the cathode surface, which effectively facilitates deprotonation and phase transfer of NH_4^+ to gaseous NH_3 . Our study aims to rationalize the design of this cathodic solid–gas–liquid reaction interface to enable simultaneous NO_3^- reduction and NH_3 extractions, which is not well studied or reported previously.

To capture NH_3 gas, the external acid or buffer solutions (e.g., H_2SO_4) must be used, which increases the cost and hazard risk or disposal issues.^{26–28} Moreover, the oxygen evolution reaction such as water oxidation at the anode is only employed as a sacrificial half-reaction to provide protons and electrons for various cathodic reactions, such as H_2 production or NO_3^- reduction.^{20,26} The anodic water oxidation consumes high electricity due to the high thermodynamic potential (e.g., 0.815 V vs NHE) and overpotential. Thus, properly redirecting the side reaction product H_2 from the cathode into the anodic chamber could potentially shift the water oxidation to H_2 oxidation (−0.414 V vs NHE) and thus decrease the total cell voltage and energy consumption. The paired electrolysis between cathodic and anodic electrochemical half-reactions deserves further research to optimize multiple mass flow balances of NO_3^- reduction, NH_3 transfer processes, proton production, and transfer to the anode.

This study demonstrates the first prototype electrified membrane system for synchronizing electrochemical NO_3^- reduction and upcycling into NH_3 without any external chemical addition. Unlike the widely reported sacrificial half-reactions in the electrochemical nitrogen recovery, paired electrolysis was employed to enable proton and hydrogen transfer between cathodic and anodic chambers to minimize energy consumption and avoid the use of acid/base for NH_3 capture and conversion. Synthetic wastewater containing NO_3^- and Cl^- was fed into the electrochemical membrane flow-cell, which consists of three reactive chambers, cathodic, anodic, and trap chambers. A CuO catalytic layer was fabricated and deposited onto the Cu foam that was attached to the polytetrafluoroethylene (PTFE) membrane to achieve cathodic NO_3^- reduction and alkalinity production for NH_4^+ deprotonation. This CuO electrocatalyst was chosen because of its fast reduction kinetics of nitrate to nitrite (a rate-limiting step for the overall reduction reaction of nitrate) and a high catalytic activity toward the production of ammonia instead of nitrogen gas.²⁹ The 3D electrode could provide a multidimensional electron transport avenue, high diffusion efficiency, and allow sustainable decentralized ammonia recovery.³⁰ The produced NH_3 transferred across the porous PTFE membrane and dissolved into the stream in the trap chamber, which was acidified by the anodic oxygen evolution reaction. The impacts of operational parameters (e.g., cathodic potentials) and water chemistry (the draw solution's pH and NO_3^- concentrations) on total nitrogen removal efficiency, NH_3 recovery efficiency, Faradic efficiency, and energy consumption for NH_3 recovery were examined. Density functional theory (DFT) calculations were undertaken to unravel the *in situ* valence state reconstruction of the CuO catalytic layer during the electrochemical NO_3^- reduction process. The presented modular electrified membrane system demonstrated the potential of nitrogen pollution conversion and resource utilization with high economic viability and sustainability.

2. MATERIALS AND METHODS

2.1. Cathodic Catalyst Layer Preparation. Cu foams (3 cm × 3 cm) with purity >99.99%, a pore density of 130 ppi (pores per linear inch), and a thickness of 0.7 mm were purchased from Kunshan Guangjiayuan New Material Co., Ltd (China) and pretreated by immersion in 3 M HCl acid for 10 min to remove the oxide layer. The $\text{Cu}(\text{OH})_2$ precursor on the Cu foam was synthesized via anodic oxidation under a direct current (DC) of 30 mA for 30 min in 25 mL of 3 M NaOH solutions with another Cu foam as the counter electrode (placed about 5 cm away from the Cu foam anode). Subsequently, a CuO layer was obtained via annealing of the $\text{Cu}(\text{OH})_2$ at 300 °C for 2 h at a heating rate of 1 °C·min^{−1} under the O_2 atmosphere.

2.2. Physicochemical Characterization. X-ray diffraction (SEM) patterns were recorded using a Bruker D2 PHASER X-ray diffractometer with a 2θ angle of 10–80°. The size and morphology of the catalyst layer were characterized using a scanning electron microscope (SEM, FEI QUANTA FEG250) with beam energies of 5 and 15 kV. X-ray photoelectron spectroscopy (XPS) was conducted on a Thermo Fisher ESCALAB 250Xi spectrometer with Al K α as an X-ray source.

2.3. Electrochemical Tests of the CuO Catalyst Layer. All electrochemical tests of catalysts were carried out in an H-type reactor (Figure S1), which was separated by a Dupont Nafion 117 proton exchange membrane (PEM). The electrochemical properties of the pristine Cu foam and the CuO-coated foam were characterized in a three-electrode configuration using a CHI 660 electrochemical workstation (CH Instrument). The Cu foam or CuO-coated foams (1 cm × 1 cm), a saturated calomel electrode (SCE, +0.241 V vs SHE), and a platinum foil (1 cm × 1 cm) were used as the working electrode (cathode), the reference electrode, and the counter electrode, respectively. Electrochemical double-layer capacity (EDLC, C_{dl}) was further determined by cyclic voltammetry (CV), which was recorded within a potential range of 0.1 V around open-circuit potential (OCP) to avoid apparent faradaic processes with a scan rate (ν) of 10–50 mV·s^{−1}.³¹ The response current values (I_a and I_c) and the double-layer capacitances (C_{dl}) were determined from the CV test. The C_{dl} was calculated by eq 1 according to the current values (I_a and I_c) and regarded as an indicator of the active site number.

$$\frac{I_a - I_c}{2} = C_{dl}\nu \quad (1)$$

Electrochemical impedance spectroscopy (EIS) was conducted at the OCP of −0.40 and 0.03 V for Cu foam and CuO-coated foam, respectively, under an alternating current (AC) within the frequency range from 10⁵ to 10^{−2} Hz at an incremental change of 5 mV in a redox couple containing 5.0 mM $\text{K}_3\text{Fe}(\text{CN})_6/\text{K}_4\text{Fe}(\text{CN})_6$. Linear sweep voltammetry (LSV) polarization curves with/without NO_3^- in the circulating electrolyte were performed at a scan rate of 100 mV·s^{−1}.

2.4. Cathodic Membrane Preparation and Electrochemical Assessment. A CuO-coated foam was clipped to a flat sheet membrane (the nominal pore size: 0.45 μm) composed of a hydrophobic PTFE layer and a polypropylene (PP) substrate to construct a CuO composite cathode membrane assembly (a surface area: 4 cm²), as illustrated in Figure S2a. This composite membrane was inserted into an electrochemical flow-cell consisting of a trap, cathode, and

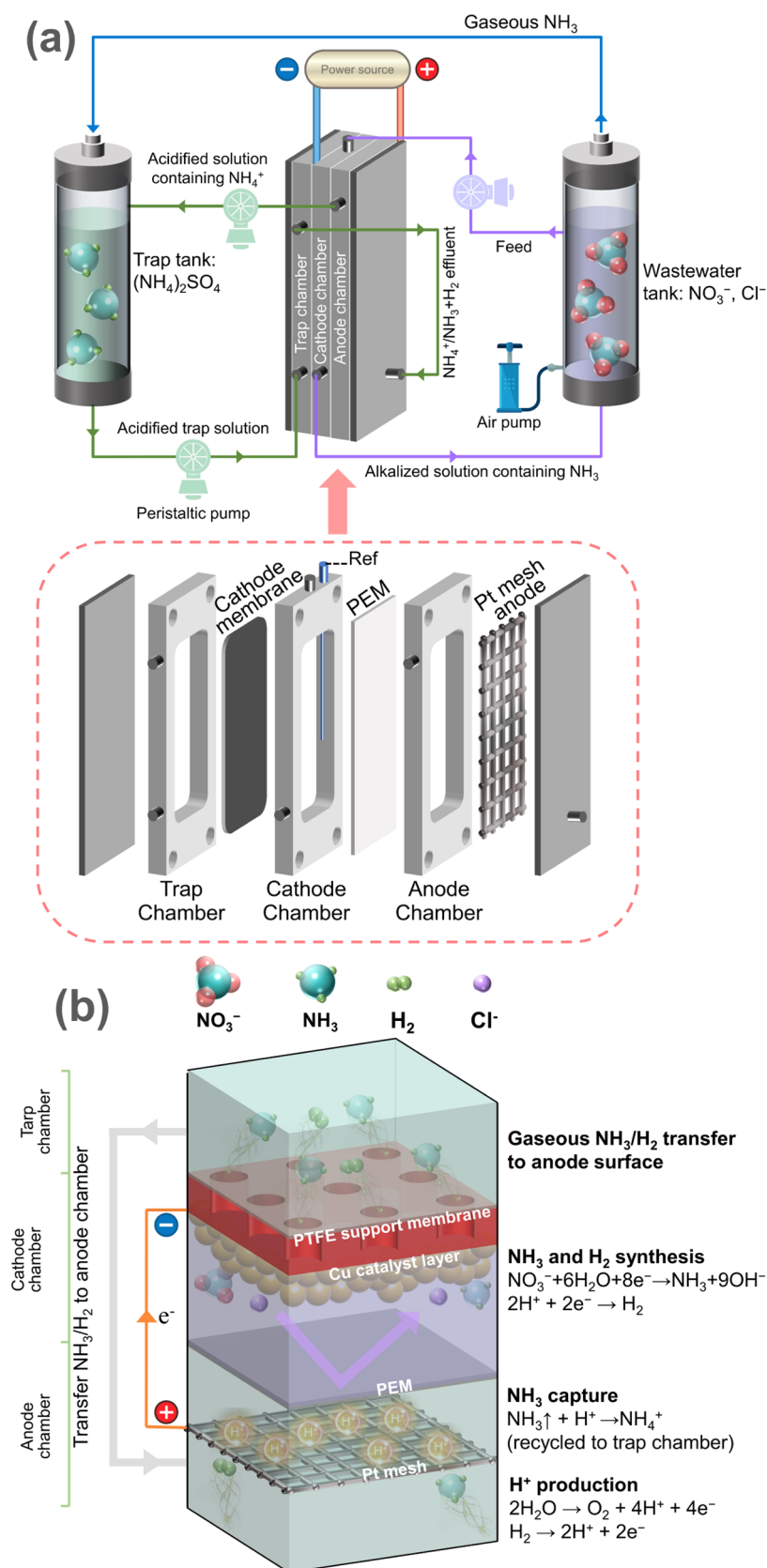


Figure 1. (a) Electrochemical flow-cell schematics. (b) The working diagram and major electrode reactions of the electrified membrane flow-cell.

anode chambers, as depicted in Figures 1a and S2b. The PP substrate and the CuO-coating layer faced the trap and cathode chambers, respectively (Figure S3). The anode and

cathode chambers were separated by the PEM to reduce the transfer of the active chlorine (HOCl or OCl^-) from the anodic chamber that may cause the oxidation of $\text{NH}_4^+/\text{NH}_3$.³²

A platinum mesh (3.5 cm × 3.5 cm) was used as an anode in the anode chamber. The SCE was connected to a CHI 1100C multichannel potentiostat (CH Instrument) to measure and control the cathodic potential. The fluid was recirculated between the three chambers and the trap or feed tanks by two peristaltic pumps (LEAD FLUIDE, BT101L) at 50 mL·min⁻¹ to promote mixing and minimize the diffusion boundary layer. For instance, an electrolyte solution (0.5 M Na₂SO₄, pH 7) was recirculated between the trap and anode chambers, while synthetic wastewater (25–150 mM NO₃⁻, 10–50 mM Cl⁻, 0.5 M Na₂SO₄, pH 7) was recirculated between the cathode chamber and the feed tank.

To determine the surface-active site reactivity of the composite cathode membrane, the relative reaction currents were collected under a constant cathodic potential (-2 V vs SCE) directly in the electrochemical flow-cell as described above with the same electrolyte conditions. The major difference is that the trap chamber was vacuumed (~4 psi) for 200 s to remove the produced H₂ and NH₃ gas through the cathode membrane and examine the potential negative effect of gas blocking on active sites and the cathodic nitrate reduction reaction. The relative reaction currents between the cathode and anode were collected in several cycles by switching vacuum on/off for 200 s respectively.

2.5. Evaluation of the Nitrate Reduction and Ammonia Recovery Using Synthetic Nitrate Feed.

2.5.1. Effects of Cathodic and Anodic Reactions on Ammonia Production. We assessed the roles of anodic reactions in acidifying the circulating electrolyte and ammonia capture by monitoring or calculating the electrolyte pH changes and the anode surface pH under different anodic potentials. Then, we compared the performances of nitrate reduction of Cu foam/PTFE membrane, CuO-coated Cu foam/PTFE membrane, and CuO-coated Cu foam only as illustrated in Figure S2c. Synthetic wastewater with/without different NaCl concentrations (10 and 50 mM) was pumped into the flow-cell with/without PEM fabrication to investigate the effect of Cl⁻ ions on ammonia production.

2.5.2. Analysis of the Cell Voltage Or Potential. The total cell voltage (E_{cell}) was measured using a multimeter (ZOYI, ZT-Y) and is primarily contributed by the cathode (E_{cathode}) and anode (E_{anode}) potentials and internal voltage losses such as ionic potential losses (E_{ionic}) and potential losses transferring the PEM (E_{transfer}) as shown in eq 2. The cathodic potential was controlled at a constant level of -2 V (vs SCE) by the potentiostat. The ionic potential losses (V) were calculated based on the measured conductivity in the cathodic and anodic compartments using eq 3. The transport losses across the PEM (V) between the anode and cathode were calculated based on the thickness and conductivity of the PEM by eq 4.

$$E_{\text{cell}} = E_{\text{cathode}} + E_{\text{anode}} + E_{\text{ionic}} + E_{\text{transfer}} \quad (2)$$

$$E_{\text{ionic}} = i \times \left(\frac{d_{\text{anode}}}{\sigma_{\text{anode}}} + \frac{d_{\text{cathode}}}{\sigma_{\text{cathode}}} \right) \quad (3)$$

$$E_{\text{transport}} = i \times \left(\frac{d_{\text{PEM}}}{\sigma_{\text{PEM}}} \right) \quad (4)$$

where i is the applied current (A·cm⁻²), d_{anode} and d_{cathode} are the thickness of the anode and cathode compartments (6 × 10⁻³ and 15 × 10⁻³ m, respectively), σ_{anode} and σ_{cathode} are the conductivity of feed media (~325 S·m⁻¹) in the anodic and

cathodic compartments, d_{PEM} is the thickness of the PEM (1.83 × 10⁻⁴ m) and σ_{PEM} is the conductivity of PEM (8.3 S·m⁻¹).

2.5.3. Effects of the Cathodic Potential, Electrolyte pH, and Input NO₃⁻-N Concentration on Ammonia Production. Various cathodic potentials (-1.5 to -3.5 V vs SCE without ohmic compensation) were applied to the cathodic membrane. Three energy efficiency indicators, the selectivity for total ammonia nitrogen (TAN), the reciprocal of EC for TAN production, and FE for TAN, were calculated and normalized by dividing the calculated results by the maximum values of each indicator. Experiments were run for 1–5 h with an initial NO₃⁻ concentration of 25 mM and under the same conditions as mentioned above in Section 2.4. The operation lasted until NO₃⁻, NO₂⁻, and TAN were barely detected in the feed tank.

Various synthetic wastewaters with different solution pHs (adjusted by adding NaOH or H₂SO₄) and NO₃⁻-N concentration were pumped into the cathodic chamber to examine the impact on the cathodic reduction of NO₃⁻ and ammonia production in the cathodic chamber, as well as ammonia recovery in the trap chamber.

2.5.4. Evaluation of the Energy Efficiency for Electrochemical Nitrate Reduction and Ammonia Production. The Faradic efficiency (FE) (%) for NH₃, N₂, and NO₂⁻ were all calculated by eq 5

$$\text{FE}(\%) = \frac{n \times F \times N_i}{Q} \times 100 \quad (5)$$

where n is the electron transfer number per mole of the reduced nitrate and is equal to 8, 5, and 2 if nitrate is reduced to NH₃, N₂, and NO₂⁻, respectively, F is the Faraday constant (96 487 C·mol⁻¹), N_i is the amount (mol) of the produced NH₃, N₂, or NO₂⁻, Q is the total charge (C) passing the electrode, which was calculated based on the integration of the curve I (A) vs t (s). In addition to the above electron transfers, cathodic H₂ production also consumed certain electrons. The partial current density toward ammonia production (j_{NH_3}) is the product of FE for ammonia production and the applied current density (I_{Total})

$$j_{\text{NH}_3} = \text{FE}(\%) \times I_{\text{total}} \quad (6)$$

The specific energy consumption (EC) (kWh·kg⁻¹-(NH₄)₂SO₄) was calculated by eq 7 to evaluate the energy cost for the produced ammonia product

$$\text{EC} = 10^{-3} \times E_{\text{cell}} \times I \times t \times m^{-1} \quad (7)$$

where E_{cell} is the total cell potential (V), $I \times t$ is the integral area under the curve I vs t (A·h) and m is the mass of the produced target (kg).

2.5.5. Determination of the Different Nitrogen Removal Efficiencies, Rates, and Selectivity. Water samples in wastewater and trap tanks were collected and filtered through 0.45-μm cellulose membranes (Millipore) to monitor different nitrogen species (e.g., ammonia and nitrate). The NO₃⁻-N removal efficiency ($R_{\text{NO}_3\text{-N}}$), total nitrogen (TN) removal efficiency (R_{TN}), NO₂⁻-N selectivity ($S_{\text{NO}_2\text{-N}}$), total ammonia nitrogen (TAN) selectivity (S_{TAN}), and N₂ selectivity (S_{N_2}) were calculated accordingly using eqs S1–S5. The NO₃⁻ removal rate (g·N·m⁻²·d⁻¹) and TAN recovery rate (g·(NH₄)₂SO₄·m⁻²·d⁻¹) were calculated based on the NO₃⁻ removal amount in the feed tank and TAN recovery amount

in the trap tank, as well as the electrode area (m^2) and overall reaction time (d). TAN recovery efficiency can be determined either by dividing the $\text{NH}_3/\text{NH}_4^+-\text{N}$ concentration in the trap tank by the initially applied NO_3^--N or by the generated $\text{NH}_3/\text{NH}_4^+-\text{N}$ if we account for the ammonia capture or stripping efficiency using eqs S6 and S7, respectively.

2.6. Assessment of Nitrate Reduction and Ammonia Recovery Using Real Wastewater. Real chemical industry wastewater was obtained from Shandong Keyuan Pharmaceutical Co., Ltd. and used to assess the nitrate reduction and ammonia recovery by our developed electrochemical flow-cell. The major components of this wastewater included NO_3^--N ($436 \pm 15 \text{ mg}\cdot\text{L}^{-1}$), Br^- ($80 \pm 3 \text{ mg}\cdot\text{L}^{-1}$), Cl^- ($214 \pm 9 \text{ mg}\cdot\text{L}^{-1}$), SO_4^{2-} ($106\,728 \pm 918 \text{ mg}\cdot\text{L}^{-1}$), Na^+ ($19\,100 \pm 523 \text{ mg}\cdot\text{L}^{-1}$), K^+ ($2447 \pm 68 \text{ mg}\cdot\text{L}^{-1}$), and chemical oxygen demand COD ($140 \pm 4 \text{ mg}\cdot\text{L}^{-1}$) with a solution pH value of 2.1 ± 0.5 . This real wastewater was pumped at the same rate ($50 \text{ mL}\cdot\text{min}^{-1}$) into the cathodic chamber and circulated back to the feed tank. The electrolyte ($0.5 \text{ M Na}_2\text{SO}_4$, pH 7) was circulated at a rate of $50 \text{ mL}\cdot\text{min}^{-1}$ between the trap and anode chambers and circulated back to the trap tank. The applied cathodic potential was -2 V vs SCE. The N-species concentrations in trap and feed tanks were monitored to assess the nitrate removal, nitrite by-product formation, and ammonia recovery.

3. RESULTS AND DISCUSSION

3.1. Morphology, Crystallinity, and Chemical State Characterization. Figure S4 shows the typical SEM images of the pristine Cu foam and the CuO-coated foam. The Cu foam exhibited a porous and relatively smooth surface. After the electric field assisted corrosion operation and subsequent high-temperature calcination, the CuO-coated foam had a rough surface covered by nanoparticles that are expected to provide a large reaction surface area and numerous active sites. The X-ray diffraction (XRD) and X-ray photoelectron spectra (XPS) verified the crystallinity and chemical binding states. For instance, the metallic Cu planes in Figure S5 are attributed to the presence of the Cu foam substrate (JCPDS no. 04-0836). The additional XRD peaks of CuO-coated foam at 2θ of 36.5° , 42.2° , and 61.4° are assigned to the (111), (200), and (220) lattice planes of the Cu_{2+1}O phase (JCPDS no. 05-0667, a copper oxide containing Cu^{2+} and Cu^{1+}), respectively.³³ As shown in Figure S6, the Cu species on the Cu mesh are mainly metallic Cu with a $6 \pm 0.3\%$ Cu^{2+} species. After corrosion and oxidation treatment, Figure 4b reveals evident XPS peaks for Cu^{2+} (953.5 eV and 933.7 eV for Cu $2p_{1/2}$ and Cu $2p_{3/2}$, respectively) and a weaker peak of Cu^0 or Cu^{1+} (951.9 and 932.1 eV for Cu $2p_{1/2}$ and Cu $2p_{3/2}$, respectively),³⁴ indicating a metallic and oxidized form of Cu. The surface Cu^{2+} species ratio in the mixed-valence catalyst layer is estimated at $95.4 \pm 2.4\%$ based on the peak area ratio for elements.

3.2. Electrochemical Characterization. Figure S7a,b are the CV curves obtained on Cu foam and Cu-coated foam. The electric double-layer capacitances (C_{dl}) of these two foams were obtained by eq 1 using the linear fitting of the charging currents and the scan rate in Figure S7c. Accordingly, the C_{dl} value of the Cu foam and CuO-coated foam are 0.21 and $0.83 \text{ mF}\cdot\text{cm}^{-2}$, respectively, indicating that CuO elicited more active sites. Furthermore, Nyquist plots and the corresponding equivalent circuits obtained in EIS analysis are shown in Figure S8a. The interfacial impedance of the Cu or CuO solids consists of an electrolyte resistance (R_s), a charge transport

resistance at the electrode–electrolyte interface (R_1), and a charge transfer resistance within the electrode (R_2).^{35,36} Clearly, the electrolyte resistance (R_s) was barely affected by the electrolyte types and thus remained almost the same (6.2 ± 0.1 and $5.8 \pm 0.0 \text{ }\Omega\cdot\text{cm}^{-2}$ for the CuO cathode and Cu foam, respectively). However, the charge transport resistances at the electrode–electrolyte interface and within the electrode (R_1 and R_2) are sensitive to the chemical changes at the interface. The CuO foam had lower charge transport resistances ($R_1 = 97.5 \pm 0.4 \text{ }\Omega \text{ cm}^{-2}$ and $R_2 = 8.5 \pm 0.9 \text{ }\Omega \text{ cm}^{-2}$) at the electrolyte/solid interface as compared to those of the Cu foam ($R_1 = 209.2 \pm 9.8 \text{ }\Omega \text{ cm}^{-2}$ and $R_2 = 19.7 \pm 0.9 \text{ }\Omega \text{ cm}^{-2}$), probably because the mixed-valence CuO layer has a higher affinity toward the electrolyte as indicated by the contact angles in Figure S9 and thus effectively decreases the accumulation of charge on the electrode surface.³⁵ In addition, the C_{dl} values were obtained by the capacitance at the electrode–electrolyte interface (Q_1) in the EIS equivalent circuit fitting,³⁷ which yields 0.92 mF cm^{-2} for the CuO cathode and 0.35 mF cm^{-2} for Cu foam, respectively. These results agree with the data from the CV test. Finally, Figure S8b shows the response current with/without NO_3^- in the electrolyte via LSV analysis, which indicates that CuO had an increased response current density in the presence of NO_3^- , indicative of a higher electrocatalytic activity for nitrate reduction than the Cu foam. Considering the different number of active sites available on CuO and Cu foam cathodes, the LSV curves were further normalized by the electric double-layer capacitances to evaluate the electroactivity for the single active site toward nitrate reduction (Figure S8c). In conclusion, the higher nitrate reduction electrocatalytic activity of the CuO cathode shown in LSV tests originates from more active sites, lower interfacial impedance, and higher intrinsic catalytic activity of the single active site.

3.3. Evaluation of Nitrate Reduction via this Flow-Through Electrified Membrane Device. **3.3.1. Anodic Reactions and Roles for Ammonia Capture.** Figures 1b and S10 show the major electrode reactions that are anticipated. For instance, the anode oxidation of the water or oxygen evolution reaction is expected to produce protons (H^+) that decrease the anodic interfacial and electrolyte pH, and then promote ammonia gas stripping and transformation into ammonium salts or $(\text{NH}_4)_2\text{SO}_4$ in this study. The anode interfacial pH was calculated by eq 8 according to Faraday's and Fick's laws.³⁸

$$j = (1000Fm_{\text{OH}}10^{\text{pH}^b - \text{pH}^*}) \left(1 - 10^{\text{pH}^* - \text{pH}^b} \right) + (1000Fm_{\text{H}}10^{-\text{pH}^b}) \left(10^{\text{pH}^b - \text{pH}^*} - 1 \right) \quad (8)$$

where j is the overall transport current ($\text{A}\cdot\text{m}^{-2}$), F is the Faraday constant ($96485 \text{ C}\cdot\text{mol}^{-1}$). $m_{\text{H}} = D_{\text{H}}/\delta_{\text{N}}$ ($\text{m}\cdot\text{s}^{-1}$) and $m_{\text{OH}} = D_{\text{OH}}/\delta_{\text{N}}$ ($\text{m}\cdot\text{s}^{-1}$), where D_{H} and D_{OH} are the diffusion coefficients of H^+ and OH^- (7.3×10^{-9} and $4.9 \times 10^{-9} \text{ m}^2\cdot\text{s}^{-1}$, respectively), the diffusion layer thicknesses (δ_{N}) of H^+ and OH^- of 24.5 and $21.5 \text{ }\mu\text{m}$, respectively, were employed for calculation as calculated by the Levich equation.³⁸ pH^b and pH^* are the pH of the bulk solution and electrode interface, $\text{p}K_w$ is the logarithm of the ionization constant of water (14). Figure S11 shows that the anode interfacial pH could be reduced appreciably when increasing the anodic potentials or anodic current. In our experiments, an anodic current density of $\sim 50 \text{ mA}\cdot\text{cm}^{-2}$ was observed with a fixed cathodic potential of -2 V vs SCE, where the anodic interfacial pH was less than

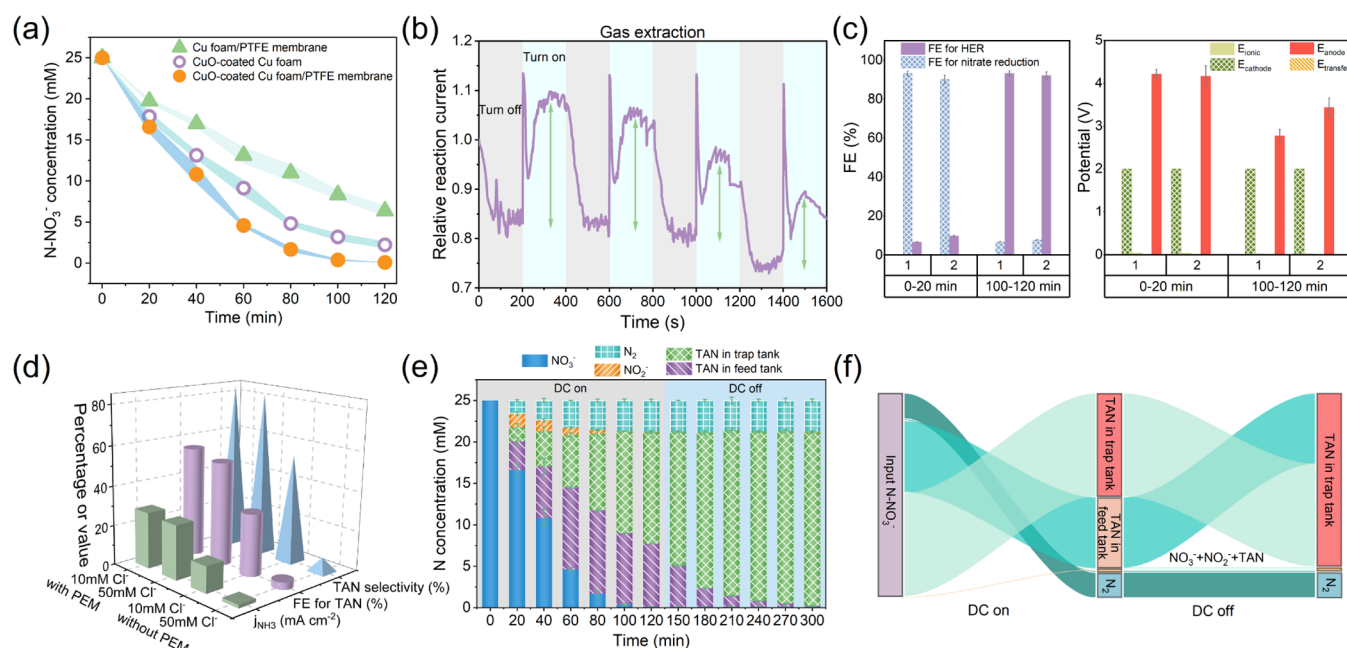


Figure 2. (a) The comparison of NO_3^- reduction by three different cathode materials: Cu foam/PTFE membrane, CuO-coated Cu foam, and CuO-coated Cu foam/PTFE membrane. The shadow area in the figure represents the error scale. A cathodic potential of -2 V vs SCE (without ohmic compensation) was carried out. Specific testing conditions: Initial NO_3^- concentration: 25 mM; pH, ~ 7.0 ; Cl^- : 10 mM; and other conditions are mentioned in Section 2.4. (b) Relative reaction currents with intermittent gas extraction by vacuuming the trap chamber. (c) Faraday efficiency (FE) and cell potential variations at different stages of reaction and with/without transferring H_2 to the anode. Numbers 1 and 2 represent with and without H_2 transfer to the anode. (d) The TAN selectivity, FE for TAN production, and partial current density toward NH_3 production (j_{NH_3}) of different Cl^- concentrations and with/without placing PEM between the anode and cathode. (e) The evolution trends of various N-species concentrations at different times. (f) The distributions of nitrogen-containing products within different operation stages.

2 and the bulk electrolyte pH progressively decreased (to 1.5–2 after 2-h operation) after passing through the anodic chamber. Thus, the stripped gaseous ammonia in the trap chamber was effectively converted into ammonium ions (NH_4^+) once passing through the anodic chamber according to this formula, $[\text{NH}_4^+]/[\text{NH}_4^+ + \text{NH}_3] = 1 - 10^{\text{pH}}/(e^{21.3} + 10^{\text{pH}})$.¹⁴ Under the local pH value decrease in the Nernstian diffusion layer near the anode surface and the acidic conditions in the anode chamber, direct ammonia oxidation is negligible because the actual reactant is NH_3 while NH_4^+ cannot be oxidized directly at the anode.^{32,39,40} This can be confirmed by the nitrogen mass balance that indicates that 78.7–87.9% input NO_3^- -N was converted into TAN.

3.3.2. Cathodic NO_3^- Reduction and the Importance of Gas Extraction. In the cathodic chamber, the nitrate reduction into ammonia was achieved via the cathodic reaction on the catalyst layer of the Cu foam as shown in Figure 1b. Moreover, the concurrent hydrogen evolution reaction and NO_3^- reduction reactions on the cathode under a cathodic current density of ~ 50 $\text{mA}\cdot\text{cm}^{-2}$ rapidly increased the cathodic interfacial pH to over 12 (Figure S11). As a result, the generated TAN on the cathode surface was nearly 100% of NH_3 , which further facilitated the transfer across the PTFE membrane and sequestration in the electrolyte of the trap chamber. Figure 2a compares the nitrate reduction rates of three cathodic environments when the nitrate (25 mM) solution flew across the same area of the cathode. The Cu foam/PTFE membrane and the CuO-coated Cu foam/PTFE membrane yielded the pseudo-first-order kinetic constants (k_{ap}) of 0.010 and 0.038 min^{-1} , respectively, further confirming superior electrocatalytic activity of the mixed-valence copper catalyst for nitrate reduction. As a comparison, when we

removed the trap chamber or ammonia stripping and only placed the CuO-coated Cu foam in contact with the nitrate solution, the k_{ap} level decreased to 0.021 min^{-1} , primarily because of the accumulation and blocking effect of the produced ammonia or hydrogen gas on the active sites. To further demonstrate the impacts of the NH_3/H_2 gas separation from the cathode on NO_3^- reduction, the reaction current response of the CuO-coated Cu foam/PTFE membrane was monitored and shown in Figure 2b, which shows a periodic oscillation of the relative current intensity as the gas extraction was enabled (vacuum) or disabled (non-vacuum or under an ambient pressure). When the vacuum was on, the efficient gas extraction led to a higher relative reaction current, suggesting that the gas extraction or gas removal from the active sites of the catalyst is critical for nitrate reduction.

3.3.3. Analysis of the Cathodic H_2 Contribution to the Reduction of the Overall Cell Potential. The cathodic H_2 production is usually inevitable and may also compete with reaction sites with nitrate reduction. However, circulating the cathodic discharge to the anode chamber could provide additional electron donors and shift water oxidation (0.815 V vs NHE) to H_2 oxidation (-0.414 V vs NHE), which ultimately reduces the total cell potential and the energy consumption. To verify this speculation, we analyzed the total cell voltage and the major components, namely, the internal potential losses or transport losses across the PEM separating cathode and anode chamber (E_{transfer}), ionic potential losses (E_{ionic}), and the potential of the anode (E_{anode}) and cathode (E_{cathode}) in the reactor at different reaction periods.^{41,42} Figure 2c reveals that compared with E_{anode} or E_{cathode} , E_{transfer} and E_{ionic} were both negligible. During the first 20 min of the overall reaction, the FE of NO_3^- reduction was 92.2–93.3%

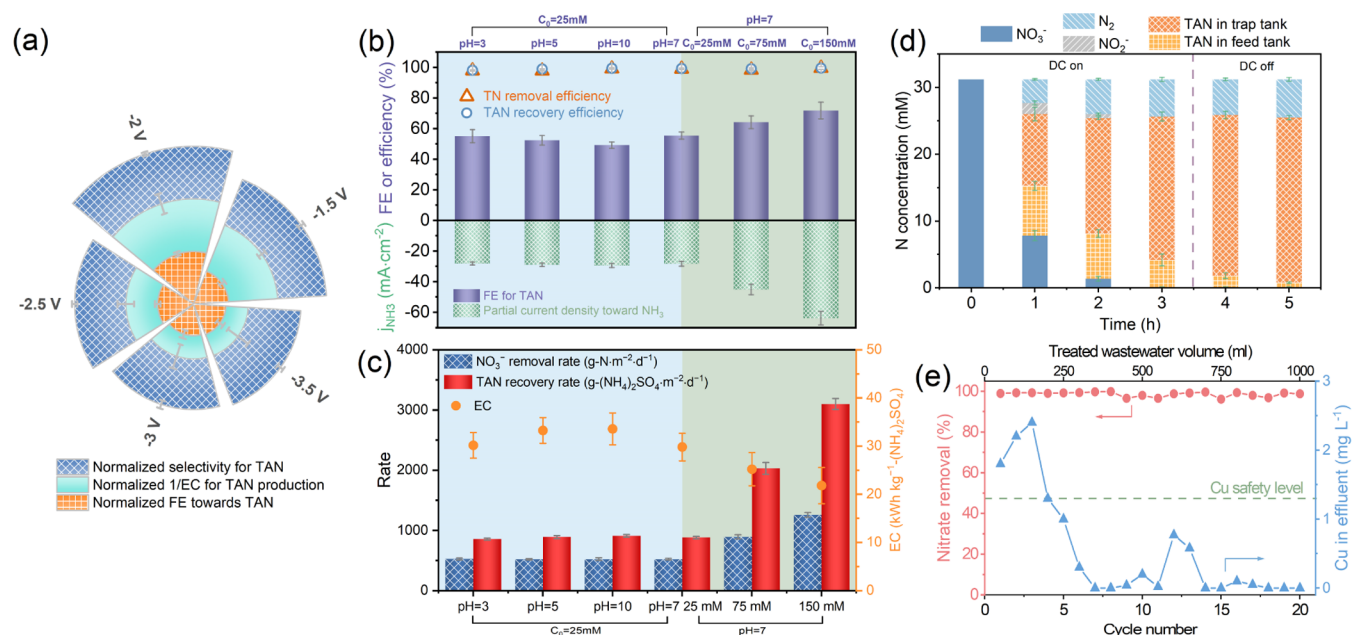


Figure 3. (a) The variations of normalized selectivity, 1/EC and FE toward TAN production under different cathodic potentials. (b) FE for TAN, partial current density toward TAN, TN removal efficiency, and TAN recovery efficiency at different solution pHs and the NO_3^- concentrations. (c) NO_3^- removal rate, TAN recovery rate, and EC at different solution pHs and the feed NO_3^- concentrations. (d) The evolution of various N-species over time of actual chemical industrial wastewater. (e) NO_3^- removal and the leached Cu concentration in the effluent as functions of operation cycles. Testing conditions are shown in Section 2.4 (NO_3^- concentration, 25 mM; pH, ~ 7.0 ; Cl^- , 10 mM; cathodic potential, -2 V vs SCE; reaction time, 2.0 h per cycle).

with a small amount of H_2 and H^+ production, leading to a total cell potential of approximately $\sim 6.2 \pm 0.1$ V and E_{anode} of $\sim 4.2 \pm 0.1$ V with/without H_2 transfer to the anode surface. However, the total cell voltage and E_{anode} both decreased in the last 20 min, primarily due to the H^+ transport rather than non-proton cations through the PEM as the anode produced a high H^+ concentration during the last 20 min. This proton migration may have reduced the ionic transport resistance and thus the total cell potential,⁴³ as indicated by the reduced cell potential from 6.2 ± 0.1 V (first 20 min) to 5.5 ± 0.2 V (last 20 min) when H_2 did not reach the anode. Furthermore, when examining the E_{anode} during the last 20 min, as the FE of H_2 production increased to 90.2–93.2% owing to the reduced available NO_3^- , E_{anode} further reduced from 3.4 ± 0.2 V (without much H_2 near the anode) to 2.7 ± 0.1 V (with more H_2 transferred to the anode), due to the H_2 oxidation on the anode. As a result of the transfer of H_2 to the anode, the cell potential reduction (5.93 ± 0.3 to 5.39 ± 0.2 V) further reduced the specific energy consumption from $32.8 \text{ kWh}\cdot\text{kg}^{-1}\cdot(\text{NH}_4)_2\text{SO}_4$ to $29.8 \text{ kWh}\cdot\text{kg}^{-1}\cdot(\text{NH}_4)_2\text{SO}_4$.

3.3.4. Effects of Cl^- Ions on Ammonia Production with/without PEM. Figure 2d shows that in the absence of the PEM, the TAN selectivity, faradic efficiency (FE), and partial current density toward NH_3 production (j_{NH_3}) all decreased with the Cl^- concentration increasing from 10 to 50 mM in the feed tank. By contrast, when the PEM was inserted between the cathode and anode, the active chlorine evolution on the anode was largely prevented as PEM does not permit the transfer of chlorine ions. As a result, the TAN selectivity, FE for TAN, and j_{NH_3} increased from 7.1%, 3.6%, and 1.7 mA cm^{-2} to 82.6%, 52.1%, and 27.4 mA cm^{-2} , respectively, when Cl^- was 50 mM.

3.3.5. NO_3^- Upcycling into Ammonia from Synthetic Wastewater. Figure 2e shows the concentration changes of

different nitrogen species over time under a constant cathodic potential of -2 V vs SCE with a response current density of $\sim 50 \text{ mA}\cdot\text{cm}^{-2}$. Nearly 100% NO_3^- was reduced into ammonia within 100 min of operation. Some of the produced TAN returned to the feed tank. But with continuous circulation, TAN was progressively transferred into the trap tank over time as indicated by the changes of the green and purple bars. Eventually, 63.8% of TAN-N was recovered with the remaining NO_3^- at 0.09 ± 0.03 mM, NO_2^- at 0.03 ± 0.02 mM, and NH_4^+ at 7.63 ± 0.13 mM in the cathode chamber with the rest of nitrogen ending up as nitrogen (N_2) gas after 120 min of operation. In addition, the NH_3 gas accounted for nearly 100% of TAN due to the high electrolyte pH (12.65 ± 0.13) in the trap chamber.¹⁴ Thus, after 120 min, the DC power was turned off as there was no more nitrate reduction and also not much of the remaining NH_4^+ ions that require deprotonation in the cathodic chamber. The residual NH_3 gas in the cathodic chamber spontaneously passed through the membrane driven by the pH gradient and/or the ammonia vapor pressure difference, and was finally fixed as $(\text{NH}_4^+)_2\text{SO}_4$ in the trap chamber. The H^+ production on the anode was also terminated when the DC power was off. Our calculation indicates that the total amount of the H^+ generated at the anode within the first 120 min was 15.2 ± 0.8 mmol (0.204 ± 0.011 A) with a final trap tank solution pH of 1.53 ± 0.10 . The total molar amount of the generated NH_3 was only 1.05 mmol, implying that the remaining H^+ in the trap and anode chambers was sufficient to protonate the remaining NH_3 (7.63 ± 0.13 mM) in the feed tank (50 mL).²⁷ After a 3-h operation (e.g., circulating the flows through, the trap, cathodic, and anodic chambers), 99.3% of the generated TAN was recovered with only 0.15 ± 0.03 mM TAN remaining in the feed tank. In addition, the trap tank can be repetitively used to recover and

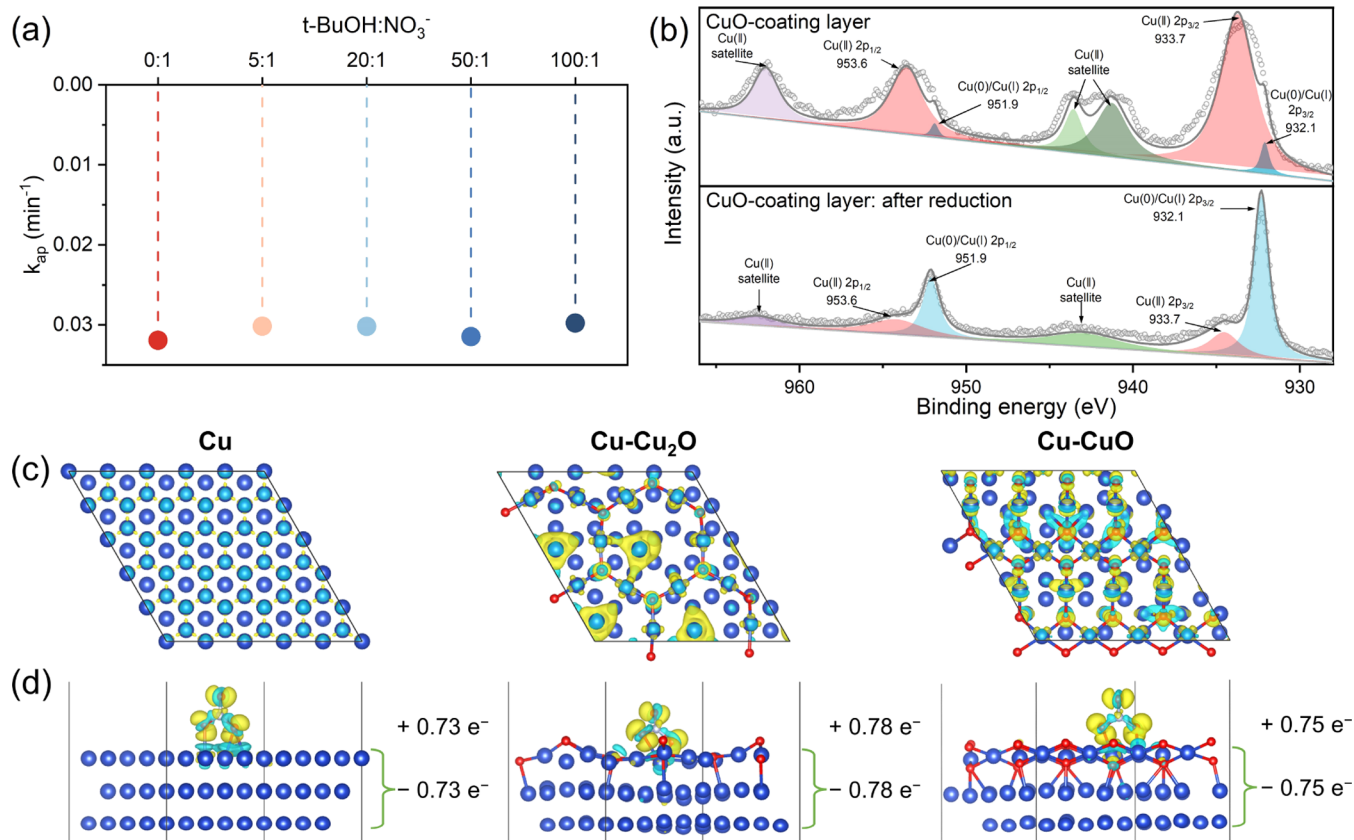


Figure 4. (a) First-order rate constant ratio with different t-BuOH:NO₃[−] molar concentration ratios. (b) XPS spectra of the CuO-coating layer before and after 2 h of electrolysis under -2 V vs SCE cathodic potential. Isosurfaces of differential charge density ($\Delta\rho$) (yellow: electron accumulation; cyan: electron depletion); (c) (111) surface of Cu, Cu-Cu₂O, and Cu-CuO ($\Delta\rho = \rho_{\text{total}} - \rho_{\text{the first layer}} - \rho_{\text{the second and third layer}}$) (isovalue = $0.005 \text{ e}/\text{\AA}^3$); and (d) NO₃[−] adsorbed on the surface of Cu, Cu-Cu₂O, and Cu-CuO ($\Delta\rho = \rho_{\text{total}} - \rho_{\text{nitrate}} - \rho_{\text{substrate}}$) (isovalue = $0.003 \text{ e}/\text{\AA}^3$). The numbers in the figure are the electrons lost ($-e^-$) or gained ($+e^-$) by NO₃[−] or the corresponding layers.

concentrate (NH₄)₂SO₄ from multiple rounds of nitrate wastewater treatment (Figure S12).

Figure 2f shows the mass flows and species distributions in the first 120 min (with DC power) and the second 180 min operation (without DC power). After a 5-h operation, the nitrate ions were removed by over 99% with some trace residual nitrogen of $0.27 \pm 0.02 \text{ mM}$ (NO₃[−], NO₂[−], and NH₃/NH₄⁺). Moreover, nitrogen recovery rates of 83.6 and 99.3% were obtained for the recovered TAN over the total NO₃[−]-N feed and the recovered TAN over the total generated TAN, respectively. Moreover, the results indicate that the rate of NO₃[−] reduction to ammonia ($443 \pm 11 \text{ g}\cdot\text{N}\cdot\text{m}^{-2}\cdot\text{d}^{-1}$) is much higher than that of ammonia transfer or stripping ($176 \pm 10 \text{ g}\cdot\text{N}\cdot\text{m}^{-2}\cdot\text{d}^{-1}$), which requires future work to properly design the electrochemical membrane or operate the DC supply to synchronize the two processes with continuous DC power. Furthermore, the productions of H⁺ or OH[−] on the anode and cathode are also worth further optimizations to enable chemical-free and efficient ammonia capture and stripping.

3.4. Investigation of Operational Parameter, Water Chemistry, and Actual Wastewater Performance. Many operational parameters (e.g., applied cathodic/anodic potentials) and water chemistry parameters (e.g., electrolyte pH and NO₃[−] concentration) affect nitrate reduction and ammonia stripping. Figure 3a is a Nightingale diagram that compares the TAN selectivity, 1/EC, and FE for TAN production under different cathodic potentials with the detailed experimental results of nitrogen species concentrations in Figure S13. Larger

pie areas indicate higher sum values of the three energy efficiency indicators. Apparently, a cathodic potential of -2 V vs SCE (without ohmic compensation) rendered the highest TAN selectivity of 84.7%, EC of $29.8 \pm 2.87 \text{ kWh}\cdot\text{kg}^{-1}$ -(NH₄)₂SO₄, and FE of 55.4%. The TAN selectivity (78.7–85.1%) did not vary sensitively with the cathodic potential, suggesting a wide working potential window of the copper oxide catalyst. However, the FE and EC are sensitive to the applied potential and operation time.

Synthetic wastewater with different initial pH and NO₃[−] concentrations were used as the cathode chamber feed and yielded different nitrogen species evolutions in Figure S14 and S15. Figure 3b shows that TN removal efficiency and TAN recovery efficiency were relatively stable at 97.7–99.4% and 98.1–99.5% when the value pH shifted from 3 to 10 or the initial NO₃[−] concentration increased from 25 to 150 mM, probably because the interfacial pH and the [NH₃]/[TAN] ratio on the cathode surface should barely be affected by the solution pH changes.²⁶ Similarly, FE for TAN production (49.2–55.4%) and j_{NH_3} (28.1 ± 1.0 – $29.4 \pm 1.3 \text{ mA}\cdot\text{cm}^{-2}$) did not change significantly with pH variations. However, at pH 7, both of them increased as the initial NO₃[−] concentration increased to 75 and 150 mM, which increased the cathodic reaction kinetics and thus resulted in favorable ammonia production and partial current.

Figure 3c compares the rates of NO₃[−] removal and TAN recovery, and the corresponding energy consumption (EC) at

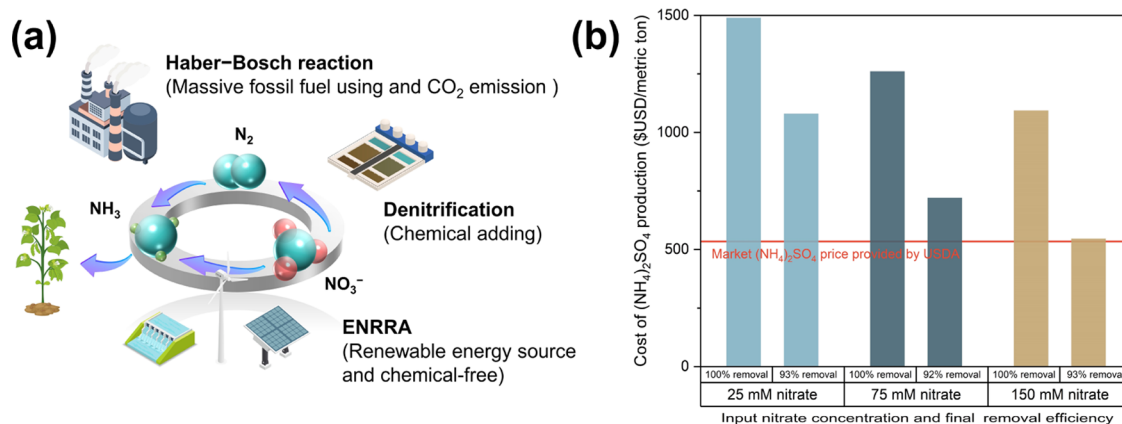


Figure 5. (a) Existing and proposed future nitrogen cycles toward nitrate removal, ammonia production, and nutrient recovery. ENRRA represents electrochemical nitrate reduction and recovery toward ammonia. (b) The electrical energy cost of (NH₄)₂SO₄ production as a function of the NO₃⁻ concentration and the removal rate, which is calculated based on electricity cost of 5 cents·kWh⁻¹.

different solution pHs and feed NO₃⁻ concentrations. Similar to the above TN removal and TAN recovery efficiencies, both removal and TAN recovery rates were barely affected by the solution pH variations. The specific EC was also stable in a range of 29.8 ± 2.9–33.5 ± 3.3 kWh·kg⁻¹·(NH₄)₂SO₄. When increasing the input NO₃⁻ concentrations to 75 and 150 mM, the NO₃⁻ removal rate increased from 894 ± 33 to 1258 ± 39 g·N·m⁻²·d⁻¹ and TAN recovery rate increased from 2030 ± 98 to 3100 ± 91 g·(NH₄)₂SO₄·m⁻²·d⁻¹, respectively. Accordingly, specific EC slightly decreased from 25.2 ± 3.5 to 21.8 ± 3.8 kWh·kg⁻¹·(NH₄)₂SO₄ due to the faster mass transfer and cathodic reactions.

Figure 3d compares the evolution of different nitrogen species over time using real wastewater. Nitrate was rapidly reduced within the first hour and converted into some N₂ and NO₂⁻ but a majority ended up as TAN in the trap and feed tank. The TAN content in the trap tank increased as ammonia or ammonium was captured as (NH₄)₂SO₄ in the trap tank. No significant NO₃⁻, NO₂⁻, or TAN in the feed tank remained after 5 h with an average rate of 436 ± 18 g·N·m⁻²·d⁻¹ for NO₃⁻ removal and 1037 ± 31 g·(NH₄)₂SO₄·m⁻²·d⁻¹ for TAN recovery, which are comparable with the results obtained using the synthesized wastewater. Clearly, this electrochemical membrane system demonstrates high tolerance against the relatively complex water matrix in actual wastewater.

To assess the long-term stability and durability of the electrocatalyst-coated membrane, Figure 3e summarizes the results of the NO₃⁻ removal and Cu concentration in the effluent over 20 operation cycles (2 h per cycle). The CuO catalyst stayed active for 20 cycles as indicated by the stable NO₃⁻ removal rate (96.6–99.9%). The leached Cu concentrations in the treated wastewater were relatively high in the initial four cycles probably because some catalysts were loosely attached to the membrane or some unreacted precursors progressively leached out. The leached Cu concentration reached a steady level of below 0.1 ppm, lower than the drinking water's maximum contamination (1.3 ppm) formulated by US EPA.⁴⁴

3.5. Analysis of the Cu Electrocatalyst and the Nitrate Reduction Mechanism. According to previous studies,^{21,22,29} direct reduction combining H⁺ bonding and electron transfer, as well as indirect reduction driven by surface-adsorbed atomic hydrogen (•H) are considered to be responsible for electrochemical NO₃⁻ reduction. To explore the effects of indirect

reduction, tertiary butanol (*t*-BuOH) was employed to scavenge and convert •H into inert 2-methyl-2-propanol radicals.^{45,46} The pseudo-first-order kinetic constants (*k*_{ap}) of NO₃⁻ reduction on the CuO-coated Cu foam/PTFE membrane remained nearly constant (0.030–0.032 min⁻¹) with the ratio of *t*-BuOH:NO₃⁻ increased from 0:1 to 100:1 (Figure 4a). This indicates that direct electron transfer coupled with the H⁺ bonding played a dominant role.

During the electrocatalytic NO₃⁻ reduction, the negative potential application will induce the valence state evolution of catalytic materials.⁴⁷ After 2 h of electrolysis under -2 V vs SCE cathodic potential, the percentage of mixed-valence states of Cu (Cu⁰, Cu¹⁺, and Cu²⁺) in the surface CuO-coating layer changed. The surface Cu²⁺ species ratio decreased from 95.4 ± 2.4% to 32.6 ± 1.7%, accompanied by an increase of Cu⁰⁺ and Cu¹⁺ species (Figure 4b). According to previous studies, the percentage of Cu⁰⁺, Cu¹⁺, and Cu²⁺ species is primarily controlled by the applied cathodic potentials rather than the reaction time.⁴⁸ The *in situ* valence state reconstruction of the CuO usually occurs within 10 min and then remains relatively stable. Thus, the mixed-valence states of Cu were stable without significant risk of over-reduction, which is supported by the stable nitrate reduction observed in Figure 3e. Density functional theory (DFT) calculations were further conducted to elucidate the mechanism of electrocatalytic NO₃⁻ reduction via direct electron transfer over Cu⁰, Cu¹⁺, and Cu²⁺ sites (see details in Section S8). According to the major exposed lattice plane in XRD analysis, Cu (111), Cu₂O (111), and CuO (111) were selected as studied reaction interfaces (Figure S16). The densities of states (DOS) of Cu, Cu-Cu₂O, and Cu-CuO interfaces near the Fermi energy are relatively high (18.4–32.8), indicating that the free-carrier densities are not affected by the introduction of Cu₂O and CuO (Figure S17).^{49,50} Thus, Cu, Cu-Cu₂O, and Cu-CuO interfaces all exhibit good electrical conductivity and ensure the transformation of electrons from the current collector or substrate into the cathode surface.⁵¹ The charge density differences of Cu, Cu-Cu₂O, and Cu-CuO surface models shown in Figure 4c illustrate the electron transfer from the Cu substrate to Cu, Cu₂O, and Cu₂O surface layers. Weak or distributed electron transfers are observed on Cu and Cu-CuO interfaces. The weak electron distribution on Cu⁰⁺ sites could explain the slow kinetics of NO₃⁻ reduction on Cu foam cathode. In contrast, massive electrons are enriched in the Cu¹⁺ site loci in the

center of the honeycomb of Cu-Cu₂O interfaces, which is 0.58 e⁻ more than that of Cu²⁺ and favorable for the electron transformation into the adsorbed NO₃⁻. We further conducted the charge density differences after adsorbing NO₃⁻ (Figure 4d). The NO₃⁻ obtained 0.73, 0.78, and 0.75 electrons from the Cu⁰, Cu¹⁺, and Cu²⁺ binding sites, respectively. Namely, the Cu¹⁺ site outperforms Cu²⁺ site with a favorable direct reduction pathway of NO₃⁻. The *in situ* electrochemically converted Cu¹⁺ from Cu²⁺ serve as high dynamic active species for NO₃⁻ reduction to NH₃.

4. ENVIRONMENTAL IMPLICATIONS

Figure 5a illustrates the synergies of combining NO₃⁻ removal and upcycling into commodity products such as an ammonia fertilizer. Our study presents the first proof of concept and validated the feasibility of such a combination via synchronizing electrochemical nitrate and ammonia's membrane stripping. This electrified membrane flow-cell system is highly scalable, modular, and free of external additions of chemicals. Compared to industrial ammonia production via the Haber-Bosch reaction, this approach dramatically reduces the cost of ammonia production and also creates multiple synergies or benefits. For example, the primary energy consumption in the Haber-Bosch and nitrification-denitrification wastewater treatment processes are typically in the range of 10 278–12 500 kWh·ton⁻¹-N and 11 722–12 500 kWh·ton⁻¹-N, respectively, which correspond to 514–625 \$·ton⁻¹-N and 586–625 \$·ton⁻¹-N based on the electricity cost of 5 cents·kWh⁻¹.⁵² According to sensitivity analysis,^{26,53} the cost of electro-synthesized (NH₄)₂SO₄ from NO₃⁻ are mainly determined by the total cell potential and faradic efficiency. A higher current efficiency was achieved at higher NO₃⁻ concentrations, resulting in a lower electricity cost. Specifically, the required electricity cost for completely/partially converting 25 and 150 mM NO₃⁻ to (NH₄)₂SO₄ was \$1490–\$547 ton⁻¹, respectively (Figure 5b). In fact, the electricity cost can be further reduced if a low NO₃⁻ removal rate is set because there is a tradeoff between the faradic efficiency and NO₃⁻ removal rate. In addition, the electrochemical recovery of (NH₄)₂SO₄ from water with high salinity needs a relatively low cell potential. These results suggest that saline wastewaters with high-strength NO₃⁻ are preferred for electrochemical upcycling of NO₃⁻ into (NH₄)₂SO₄. However, real wastewater streams such as agricultural runoffs usually have fairly low nitrate concentrations and may require a certain separation or concentration of nitrate to improve the electrochemical conversion efficiency. The obtained (NH₄)₂SO₄ may be sold as a fertilizer at a price of 533 \$·ton⁻¹ (according to USDA⁸) and further offset the cost of NO₃⁻ removal. For instance, 1666 tons (NH₄)₂SO₄/year could be produced for a medium-size water treatment plant (10 MGD) with 30 mg·L⁻¹ NO₃⁻-N removal and 85% TAN selectivity, rendering an annual revenue of \$887,978. Thus, considering its invaluable environmental and economic benefits, the electrochemical upcycling of NO₃⁻ into (NH₄)₂SO₄ outcompetes the industrial NH₃ synthesis in the Haber-Bosch process and the NO₃⁻ pollutant removal by the nitrification-denitrification process. In addition, treated water from this electrified membrane reactor yields a high pH (>12.5) that could reduce the water hardness (Ca²⁺ and Mg²⁺) and produce phosphorus-containing fertilizers (struvite, MgNH₄PO₄·6H₂O), or recover ammonia from urine/ammonium wastewater.^{54,55} Thus, this study paves a sustainable

pathway of nitrogen upcycling and demonstrates the potential to enable resource recovery from nitrate and nitrite wastewater.

■ ASSOCIATED CONTENT

Supporting Information

The Supporting Information is available free of charge at <https://pubs.acs.org/doi/10.1021/acs.est.1c08442>.

Chemicals and materials, illustration of electrochemical measurements and flow-cell setup, physicochemical characterization (including SEM images and XRD, and XPS spectra) and electrochemical analysis (including LSV, CV, and EIS) of cathodic catalyst coating, calculation of cathodic and anodic interfacial pH, analytical methods for different nitrogen species and other water quality indicators, calculations of N-species relevant efficiencies, details of electrochemical flow-cell performance in various operations (including cathodic potential, solution pHs, and NO₃⁻ concentration), Cu leaching test, and DFT calculation details (PDF)

■ AUTHOR INFORMATION

Corresponding Authors

Bo Jiang – School of Environmental and Municipal Engineering, Qingdao University of Technology, Qingdao 266033, P. R. China; orcid.org/0000-0001-9500-2145; Email: bjiang86upc@163.com

Wen Zhang – John A. Reif, Jr. Department of Civil and Environmental Engineering, New Jersey Institute of Technology, Newark, New Jersey 07102, United States; orcid.org/0000-0001-8413-0598; Email: wen.zhang@njit.edu

Authors

Jianan Gao – School of Environmental and Municipal Engineering, Qingdao University of Technology, Qingdao 266033, P. R. China; John A. Reif, Jr. Department of Civil and Environmental Engineering, New Jersey Institute of Technology, Newark, New Jersey 07102, United States; orcid.org/0000-0003-1255-1240

Ning Shi – School of Environmental and Municipal Engineering, Qingdao University of Technology, Qingdao 266033, P. R. China

Yifan Li – School of Environmental and Municipal Engineering, Qingdao University of Technology, Qingdao 266033, P. R. China; orcid.org/0000-0001-5764-5350

Taha Marhaba – John A. Reif, Jr. Department of Civil and Environmental Engineering, New Jersey Institute of Technology, Newark, New Jersey 07102, United States

Complete contact information is available at:

<https://pubs.acs.org/10.1021/acs.est.1c08442>

Author Contributions

J.G. designed and performed the experiment and wrote the original draft. N.S. prepared the catalyst. Y.L. conducted the DFT calculations. T.M. supervised the experiments. B.J. and W.Z. were responsible for supervision, conceptualization, and writing, reviewing, and editing.

Notes

The authors declare no competing financial interest.

ACKNOWLEDGMENTS

The study was financially supported by the NSF PFI-TT project and the INTERN program (Award number: 2016472) and the Natural Science Foundation of Shandong Province (Award number: ZR2021MB003, ZR2021QB205).

REFERENCES

- (1) Erisman, J. W.; Sutton, M. A.; Galloway, J.; Klimont, Z.; Winiwarter, W. How a century of ammonia synthesis changed the world. *Nat. Geosci.* **2008**, *1*, 636–639.
- (2) Guo, W.; Zhang, K.; Liang, Z.; Zou, R.; Xu, Q. Electrochemical nitrogen fixation and utilization: theories, advanced catalyst materials and system design. *Chem. Soc. Rev.* **2019**, *48*, 5658–5716.
- (3) Hao, D.; Liu, Y.; Gao, S.; Arandiyani, H.; Bai, X.; Kong, Q.; Wei, W.; Shen, P. K.; Ni, B.-J. Emerging artificial nitrogen cycle processes through novel electrochemical and photochemical synthesis. *Mater. Today* **2021**, *46*, 212–233.
- (4) Zhang, X.; Ward, B. B.; Sigman, D. M. Global Nitrogen Cycle: Critical Enzymes, Organisms, and Processes for Nitrogen Budgets and Dynamics. *Chem. Rev.* **2020**, *120*, 5308–5351.
- (5) Duca, M.; Koper, M. T. M. Powering denitrification: the perspectives of electrocatalytic nitrate reduction. *Energy Environ. Sci.* **2012**, *5*, 9726–9742.
- (6) Conley, D. J.; Paerl Hans, W.; Howarth Robert, W.; Boesch Donald, F.; Seitzinger Sybil, P.; Havens Karl, E.; Lancelot, C.; Likens Gene, E. Controlling Eutrophication: Nitrogen and Phosphorus. *Science* **2009**, *323*, 1014–1015.
- (7) Dodds, W. K.; Bouska, W. W.; Eitzmann, J. L.; Pilger, T. J.; Pitts, K. L.; Riley, A. J.; Schloesser, J. T.; Thornbrugh, D. J. Eutrophication of U.S. Freshwaters: Analysis of Potential Economic Damages. *Environ. Sci. Technol.* **2009**, *43*, 12–19.
- (8) McEnaney, J. M.; Blair, S. J.; Nielander, A. C.; Schwalbe, J. A.; Koshy, D. M.; Cargnello, M.; Jaramillo, T. F. Electrolyte Engineering for Efficient Electrochemical Nitrate Reduction to Ammonia on a Titanium Electrode. *ACS Sustainable Chem. Eng.* **2020**, *8*, 2672–2681.
- (9) Guest, J. S.; Skerlos, S. J.; Barnard, J. L.; Beck, M. B.; Daigger, G. T.; Hilger, H.; Jackson, S. J.; Karvazy, K.; Kelly, L.; Macpherson, L.; Mihelcic, J. R.; Pramanik, A.; Raskin, L.; Van Loosdrecht, M. C. M.; Yeh, D.; Love, N. G. A New Planning and Design Paradigm to Achieve Sustainable Resource Recovery from Wastewater. *Environ. Sci. Technol.* **2009**, *43*, 6126–6130.
- (10) Ghimire, U.; Sarpong, G.; Gude, V. G. Transitioning Wastewater Treatment Plants toward Circular Economy and Energy Sustainability. *ACS Omega* **2021**, *6*, 11794–11803.
- (11) Greenlee, L. F. Recycling fertilizer. *Nat. Energy* **2020**, *5*, 557–558.
- (12) Wan, Y.; Huang, Z.; Zhou, L.; Li, T.; Liao, C.; Yan, X.; Li, N.; Wang, X. Bioelectrochemical Ammoniation Coupled with Microbial Electrolysis for Nitrogen Recovery from Nitrate in Wastewater. *Environ. Sci. Technol.* **2020**, *54*, 3002–3011.
- (13) Cruz, H.; Law, Y. Y.; Guest, J. S.; Rabaey, K.; Batstone, D.; Laycock, B.; Verstraete, W.; Pikaar, I. Mainstream Ammonium Recovery to Advance Sustainable Urban Wastewater Management. *Environ. Sci. Technol.* **2019**, *53*, 11066–11079.
- (14) Zhang, C.; Ma, J.; Song, J.; He, C.; Waite, T. D. Continuous Ammonia Recovery from Wastewaters Using an Integrated Capacitive Flow Electrode Membrane Stripping System. *Environ. Sci. Technol.* **2018**, *52*, 14275–14285.
- (15) Su, L.; Li, K.; Zhang, H.; Fan, M.; Ying, D.; Sun, T.; Wang, Y.; Jia, J. Electrochemical nitrate reduction by using a novel Co₃O₄/Ti cathode. *Water Res.* **2017**, *120*, 1–11.
- (16) Nguyen, T. T. P.; Do, B. K. D.; Bui, N. N.; Pham, M. A.; Nguyen, T. V. Selectiveness of Copper and Polypyrrole Modified Copper Electrodes for Nitrate Electroreduction: A Comparative Study and Application in Ground Water. *ECS Trans.* **2013**, *53*, 41–52.
- (17) Biradar, P. M.; Dhamole, P. B.; Nair, R. R.; Roy, S. B.; Satpati, S. K.; D'Souza, S. F.; Lele, S. S.; Pandit, A. B. Long-term stability of biological denitrification process for high strength nitrate removal from wastewater of uranium industry. *Environ. Prog.* **2008**, *27*, 365–372.
- (18) Huo, X.; Vanneste, J.; Cath, T. Y.; Strathmann, T. J. A hybrid catalytic hydrogenation/membrane distillation process for nitrogen resource recovery from nitrate-contaminated waste ion exchange brine. *Water Res.* **2020**, *175*, No. 115688.
- (19) Gabaldón, C.; Izquierdo, M.; Martínez-Soria, V.; Marzal, P.; Peña-roja, J.-M.; Javier Alvarez-Hornos, F. Biological nitrate removal from wastewater of a metal-finishing industry. *J. Hazard. Mater.* **2007**, *148*, 485–490.
- (20) Chen, G.-F.; Yuan, Y.; Jiang, H.; Ren, S.-Y.; Ding, L.-X.; Ma, L.; Wu, T.; Lu, J.; Wang, H. Electrochemical reduction of nitrate to ammonia via direct eight-electron transfer using a copper–molecular solid catalyst. *Nat. Energy* **2020**, *5*, 605–613.
- (21) Gao, J.; Jiang, B.; Ni, C.; Qi, Y.; Zhang, Y.; Oturan, N.; Oturan, M. A. Non-precious Co₃O₄-TiO₂/Ti cathode based electrocatalytic nitrate reduction: Preparation, performance and mechanism. *Appl. Catal. B* **2019**, *254*, 391–402.
- (22) Gao, J.; Jiang, B.; Ni, C.; Qi, Y.; Bi, X. Enhanced reduction of nitrate by noble metal-free electrocatalysis on P doped three-dimensional Co₃O₄ cathode: Mechanism exploration from both experimental and DFT studies. *Chem. Eng. J.* **2020**, *382*, No. 123034.
- (23) Li, J.; Zhan, G.; Yang, J.; Quan, F.; Mao, C.; Liu, Y.; Wang, B.; Lei, F.; Li, L.; Chan, A. W. M.; Xu, L.; Shi, Y.; Du, Y.; Hao, W.; Wong, P. K.; Wang, J.; Dou, S.-X.; Zhang, L.; Yu, J. C. Efficient Ammonia Electrosynthesis from Nitrate on Strained Ruthenium Nanoclusters. *J. Am. Chem. Soc.* **2020**, *142*, 7036–7046.
- (24) Wang, Y.; Xu, A.; Wang, Z.; Huang, L.; Li, J.; Li, F.; Wicks, J.; Luo, M.; Nam, D.-H.; Tan, C.-S.; Ding, Y.; Wu, J.; Lum, Y.; Dinh, C.-T.; Sinton, D.; Zheng, G.; Sargent, E. H. Enhanced Nitrate-to-Ammonia Activity on Copper–Nickel Alloys via Tuning of Intermediate Adsorption. *J. Am. Chem. Soc.* **2020**, *142*, 5702–5708.
- (25) Jia, R.; Wang, Y.; Wang, C.; Ling, Y.; Yu, Y.; Zhang, B. Boosting Selective Nitrate Electroreduction to Ammonium by Constructing Oxygen Vacancies in TiO₂. *ACS Catal.* **2020**, *10*, 3533–3540.
- (26) Gao, J.; Shi, N.; Guo, X.; Li, Y.; Bi, X.; Qi, Y.; Guan, J.; Jiang, B. Electrochemically Selective Ammonia Extraction from Nitrate by Coupling Electron- and Phase-Transfer Reactions at a Three-Phase Interface. *Environ. Sci. Technol.* **2021**, *55*, 10684–10694.
- (27) Kim, K.-Y.; Moreno-Jimenez, D. A.; Efstathiadis, H. Electrochemical Ammonia Recovery from Anaerobic Centrate Using a Nickel-Functionalized Activated Carbon Membrane Electrode. *Environ. Sci. Technol.* **2021**, *55*, 7674–7680.
- (28) McCartney, S. N.; Williams, N. A.; Booc, C.; Chen, X.; Yip, N. Y. Novel Isothermal Membrane Distillation with Acidic Collector for Selective and Energy-Efficient Recovery of Ammonia from Urine. *ACS Sustainable Chem. Eng.* **2020**, *8*, 7324–7334.
- (29) Garcia-Segura, S.; Lanzarini-Lopes, M.; Hristovski, K.; Westerhoff, P. Electrocatalytic reduction of nitrate: Fundamentals to full-scale water treatment applications. *Appl. Catal. B* **2018**, *236*, 546–568.
- (30) Cerrón-Calle, G. A.; Fajardo, A. S.; Sánchez-Sánchez, C. M.; Garcia-Segura, S. Highly reactive Cu-Pt bimetallic 3D-electrocatalyst for selective nitrate reduction to ammonia. *Appl. Catal. B* **2022**, *302*, No. 120844.
- (31) Xing, Z.; Hu, L.; Ripatti, D. S.; Hu, X.; Feng, X. Enhancing carbon dioxide gas-diffusion electrolysis by creating a hydrophobic catalyst microenvironment. *Nat. Commun.* **2021**, *12*, No. 136.
- (32) Zhang, C.; He, D.; Ma, J.; Waite, T. D. Active chlorine mediated ammonia oxidation revisited: Reaction mechanism, kinetic modelling and implications. *Water Res.* **2018**, *145*, 220–230.
- (33) Tong, M.; Sun, F.; Xie, Y.; Wang, Y.; Yang, Y.; Tian, C.; Wang, L.; Fu, H. Operando Cooperated Catalytic Mechanism of Atomically Dispersed Cu–N₄ and Zn–N₄ for Promoting Oxygen Reduction Reaction. *Angew. Chem. Int. Ed.* **2021**, *60*, 14005–14012.
- (34) Wang, S.; Kou, T.; Varley, J. B.; Akhade, S. A.; Weitzner, S. E.; Baker, S. E.; Duoss, E. B.; Li, Y. Cu₂O/CuS Nanocomposites Show Excellent Selectivity and Stability for Formate Generation via

Electrochemical Reduction of Carbon Dioxide. *ACS Mater. Lett.* **2021**, *3*, 100–109.

(35) Kong, Y.; Li, J.; Wang, Y.; Chu, W.; Liu, Z. Tuning Interfacial Electron Transfer by Anchoring NiFe-LDH on In-situ Grown Cu₂O for Enhancing Oxygen Evolution. *Catal. Lett.* **2020**, *150*, 3049–3057.

(36) Zeng, J.; Bejtka, K.; Ju, W.; Castellino, M.; Chiodoni, A.; Sacco, A.; Farkhondehfar, M. A.; Hernández, S.; Rentsch, D.; Battaglia, C.; Pirri, C. F. Advanced Cu-Sn foam for selectively converting CO₂ to CO in aqueous solution. *Appl. Catal. B* **2018**, *236*, 475–482.

(37) Zhu, Q.; Hinkle, M.; Kim, D. J.; Kim, J.-H. Modular Hydrogen Peroxide Electrosynthesis Cell with Anthraquinone-Modified Polyaniline Electrocatalyst. *ACS ES&T Eng.* **2021**, *1*, 446–455.

(38) Yin, F.; Liu, H. The j–pH diagram of interfacial reactions involving H⁺ and OH[–]. *J. Energy Chem.* **2020**, *50*, 339–343.

(39) Fajardo, A. S.; Westerhoff, P.; Sanchez-Sanchez, C. M.; Garcia-Segura, S. Earth-abundant elements a sustainable solution for electrocatalytic reduction of nitrate. *Appl. Catal. B* **2021**, *281*, No. 119465.

(40) Zöllig, H.; Morgenroth, E.; Udert, K. M. Inhibition of Direct Electrolytic Ammonia Oxidation Due to a Change in Local pH. *Electrochim. Acta* **2015**, *165*, 348–355.

(41) Kuntke, P.; Rodríguez Arredondo, M.; Widyakristi, L.; ter Heijne, A.; Sleutels, T. H. J. A.; Hamelers, H. V. M.; Buisman, C. J. N. Hydrogen Gas Recycling for Energy Efficient Ammonia Recovery in Electrochemical Systems. *Environ. Sci. Technol.* **2017**, *51*, 3110–3116.

(42) Kuntke, P.; Rodrigues, M.; Sleutels, T.; Saakes, M.; Hamelers, H. V. M.; Buisman, C. J. N. Energy-Efficient Ammonia Recovery in an Up-Scaled Hydrogen Gas Recycling Electrochemical System. *ACS Sustainable Chem. Eng.* **2018**, *6*, 7638–7644.

(43) Yang, Y.; Lin, L.; Tse, L. K.; Dong, H.; Yu, S.; Hoffmann, M. R. Membrane-separated electrochemical latrine wastewater treatment. *Environ. Sci. Water Res. Technol.* **2019**, *5*, 51–59.

(44) Xu, J.; Zheng, X.; Feng, Z.; Lu, Z.; Zhang, Z.; Huang, W.; Li, Y.; Vuckovic, D.; Li, Y.; Dai, S.; Chen, G.; Wang, K.; Wang, H.; Chen, J. K.; Mitch, W.; Cui, Y. Organic wastewater treatment by a single-atom catalyst and electrolytically produced H₂O₂. *Nat. Sustainable* **2021**, *4*, 233–241.

(45) Mao, R.; Li, N.; Lan, H.; Zhao, X.; Liu, H.; Qu, J.; Sun, M. Dechlorination of Trichloroacetic Acid Using a Noble Metal-Free Graphene–Cu Foam Electrode via Direct Cathodic Reduction and Atomic H^{*}. *Environ. Sci. Technol.* **2016**, *50*, 3829–3837.

(46) Yanan, S.; Xing, X.; Yue, Q.; Gao, B.; Li, Y. Nitrogen-doped carbon nanotubes encapsulating Fe/Zn nanoparticles as a persulfate activator for sulfamethoxazole degradation: role of encapsulated bimetallic nanoparticles and nonradical reaction. *Environ. Sci. Nano* **2020**, *7*, 1444–1453.

(47) Lyu, Z.; Zhu, S.; Xie, M.; Zhang, Y.; Chen, Z.; Chen, R.; Tian, M.; Chi, M.; Shao, M.; Xia, Y. Controlling the Surface Oxidation of Cu Nanowires Improves Their Catalytic Selectivity and Stability toward C²⁺ Products in CO₂ Reduction. *Angew. Chem. Int. Ed.* **2021**, *60*, 1909–1915.

(48) Yuan, X.; Chen, S.; Cheng, D.; Li, L.; Zhu, W.; Zhong, D.; Zhao, Z.-J.; Li, J.; Wang, T.; Gong, J. Controllable Cu⁰–Cu⁺ Sites for Electrocatalytic Reduction of Carbon Dioxide. *Angew. Chem. Int. Ed.* **2021**, *60*, 15344–15347.

(49) Gaul, C.; Hutsch, S.; Schwarze, M.; Schellhammer, K. S.; Bussolotti, F.; Kera, S.; Cuniberti, G.; Leo, K.; Ortman, F. Insight into doping efficiency of organic semiconductors from the analysis of the density of states in n-doped C60 and ZnPc. *Nat. Mater.* **2018**, *17*, 439–444.

(50) Chen, C.; Ma, Q.; Liu, F.; Gao, J.; Li, X.; Sun, S.; Yao, H.; Liu, C.; Young, J.; Zhang, W. Photocatalytically reductive defluorination of perfluorooctanoic acid (PFOA) using Pt/La₂Ti₂O₇ nanoplates: Experimental and DFT assessment. *J. Hazard. Mater.* **2021**, *419*, No. 126452.

(51) Zhang, R.; Yuan, Q.; Ma, R.; Liu, X.; Gao, C.; Liu, M.; Jia, C.-L.; Wang, H. Tuning conductivity and magnetism of CuFe₂O₄ via cation redistribution. *RSC Adv.* **2017**, *7*, 21926–21932.

(52) Van der Hoek, J. P.; Duijff, R.; Reinstra, O. Nitrogen Recovery from Wastewater: Possibilities, Competition with Other Resources, and Adaptation Pathways. *Sustainability* **2018**, *10*, 4605.

(53) De Luna, P.; Hahn, C.; Higgins, D.; Jaffer Shaffiq, A.; Jaramillo Thomas, F.; Sargent Edward, H. What would it take for renewably powered electrosynthesis to displace petrochemical processes? *Science* **2019**, *364*, No. eaav3506.

(54) Kékedy-Nagy, L.; Abolhassani, M.; Perez Bakovic, S. I.; Anari, Z.; Moore Ii, J. P.; Pollet, B. G.; Greenlee, L. F. Electroless Production of Fertilizer (Struvite) and Hydrogen from Synthetic Agricultural Wastewaters. *J. Am. Chem. Soc.* **2020**, *142*, 18844–18858.

(55) Daguerrre-Martini, S.; Vanotti, M. B.; Rodriguez-Pastor, M.; Rosal, A.; Moral, R. Nitrogen recovery from wastewater using gas-permeable membranes: Impact of inorganic carbon content and natural organic matter. *Water Res.* **2018**, *137*, 201–210.

Recommended by ACS

Simple and Low-Cost Electroactive Membranes for Ammonia Recovery

Xinyi Wang, David Jassby, *et al.*

JUNE 15, 2023

ENVIRONMENTAL SCIENCE & TECHNOLOGY

READ 

A Bipolar Membrane-Integrated Electrochlorination Process for Highly Efficient Ammonium Removal in Mature Landfill Leachate: The Importance of ClO[•] Generation

Wenjie Kuang, Chunhua Feng, *et al.*

OCTOBER 14, 2022

ENVIRONMENTAL SCIENCE & TECHNOLOGY

READ 

Model Unraveling the Ultra-Efficient Multi-Stage Flow-Through Anodes for Water Purification Application: Development of Design and Evaluation

Min Chen, Jiuhui Qu, *et al.*

FEBRUARY 14, 2023

ACS ES&T ENGINEERING

READ 

Flow-Through Electrochemical Activation of Persulfate for Efficient Wastewater Treatment using Ti₄O₇ Reactive Electrochemical Membranes

Hanjun Peng, Hui Lin, *et al.*

APRIL 12, 2023

ACS ES&T WATER

READ 

Get More Suggestions >